Dark Off-limb Gap

Kuridze, David; Heinzel, Petr; Koza, Július; Oliver, Ramon

Published in:
The Astrophysical Journal

DOI:
10.3847/1538-4357/ac8d8e

Publication date:
2022

Citation for published version (APA):
Kuridze, D., Heinzel, P., Koza, J., & Oliver, R. (2022). Dark Off-limb Gap: Manifestation of a Temperature Minimum and the Dynamic Nature of the Chromosphere. *The Astrophysical Journal*, *937*(2), [56]. https://doi.org/10.3847/1538-4357/ac8d8e

The Astrophysical Journal, 937:56 (11pp), 2022 October 1 https://doi.org/10.3847/1538-4357/ac8d8e

Dark Off-limb Gap: Manifestation of a Temperature Minimum and the Dynamic Nature of the Chromosphere

David Kuridze[1,2], Petr Heinzel[3,4], Július Koza[5], and Ramon Oliver[6,7]
[1] Department of Physics, Aberystwyth University, Ceredigion, SY23 3BZ, UK; dak21@aber.ac.uk
[2] Abastumani Astrophysical Observatory, Mount Kanobili, 0301, Abastumani, Georgia
[3] Astronomical Institute, The Czech Academy of Sciences, 25165 Ondřejov, Czech Republic
[4] University of Wroclaw, Centre of Scientific Excellence—Solar and Stellar Activity, Kopernika 11, 51-622 Wroclaw, Poland
[5] Astronomical Institute, Slovak Academy of Sciences, 059 60 Tatranská Lomnica, Slovakia
[6] Departament de Física, Universitat de les Illes Balears, E-07122 Palma de Mallorca, Spain
[7] Institute of Applied Computing & Community Code (IAC3), UIB, Spain
Received 2021 October 25; revised 2022 August 26; accepted 2022 August 27; published 2022 September 28

Abstract

We study off-limb emission of the lower solar atmosphere using high-resolution imaging spectroscopy in the Hβ and Ca II 8542 Å lines obtained with the CHROMospheric Imaging Spectrometer (CHROMIS) and the CRisp Imaging SpectroPolarimeter (CRISP) on the Swedish 1 m Solar Telescope. The Hβ line-wing images show the dark intensity gap between the photospheric limb and chromosphere, which is absent in the Ca II images. We calculate synthetic spectra of the off-limb emissions with the RH code in one-dimensional spherical geometry and find good agreement with the observations. The analysis of synthetic line profiles shows that the gap in the Hβ line-wing images maps the temperature minimum region between the photosphere and chromosphere due to the well-known opacity and emissivity gap of Balmer lines in this layer. However, the observed gap is detected farther from the line core in the outer line-wing positions than in the synthetic profiles. We found that an increased microturbulence in the model chromosphere is needed to reproduce the dark gap in the outer line wing, suggesting that the observed Hβ gap is the manifestation of the temperature minimum and the dynamic nature of the solar chromosphere. The temperature minimum produces a small enhancement in synthetic Ca II line-wing intensities. Observed off-limb Ca II line-wing emissions show similar enhancement below the temperature minimum layer near the edge of the photospheric limb.

Unified Astronomy Thesaurus concepts: Spectroscopy (1558); Ground telescopes (687); Solar chromosphere (1479); High resolution spectroscopy (2096); Radiative transfer simulations (1967)

1. Introduction

The solar atmosphere under nonideal MHD approximation evolves as a magnetized fluid that is governed by equations of hydrodynamics representing conservation of mass, momentum, and energy. These are coupled with the radiative transfer equation and induction equation for the magnetic field. Within the three-dimensional radiation-MHD (3D R-MHD) modeling, basic parameters of the solar atmosphere such as temperature, velocity, density, and magnetic field result from solving them in the spatial and temporal domains. However, the 3D R-MHD modeling has limitations, such as ad hoc replacement of the viscosity and resistance by numerical terms that are independent of temperature (Leenaarts 2020). One of the most puzzling aspects of the solar atmosphere is breaking the radiative equilibrium in the layers above the photosphere. Therefore, deposition of nonthermal energy and conversion into heat must occur in the chromosphere and corona—thus, they are hotter than the radiative equilibrium assumes. The question of "how much hotter?" was answered by analyzing ground and space spectroscopic data acquired by various techniques.

Early solar physics utilized solar eclipses as the primary source of quantitative chromospheric data (see Judge et al. 2019 and references therein). Time series of flash spectra, acquired with high cadence in the brief moments after and before the second and third contact, respectively, yielded the first hints of the physical conditions in the chromosphere. For example, an extensive set of the high-cadence chromospheric flash spectra, obtained at the 1952 eclipse in Khartoum, was analyzed in Athay et al. (1954). Recently, high-cadence flash spectra ($\geqslant$8 ms cadence), acquired by a novel experiment during the 2017 August 21 eclipse, were studied in Judge et al. (2019).

Lack of detailed knowledge of heating mechanisms in the layers, where radiative equilibrium breaks down, forced the construction of one-dimensional (1D) semiempirical (SE) models where the temperature structure of the atmosphere (i.e., T versus the column mass or height) is inferred from long-slit spectroscopy by radiative transfer calculations assuming nonlocal thermodynamic equilibrium (non-LTE; i.e., departures from LTE). The non-LTE problem consistently takes into account the weak coupling of radiation field with the matter in the chromosphere. The 1D SE models are primarily based on on-disk observations of continua and several strong spectral lines. Temperature is the variable that most strongly controls the continuum and spectral line shapes and intensities yielded by the classical SE models (Gingerich et al. 1971; Vernazza et al. 1981; Fontenla et al. 1993; Rutten & Uitenbroek 2012; Heinzel & Štěpán 2019). This sensitivity arises from the exponential and power dependence on T in the excitation–ionization processes (Gray 2008). Their characteristic feature is a distinct temperature minimum (TM) separating the upper

photosphere, dominated by the gas pressure, from the lower chromosphere where the magnetic field gains a dominance over the gas. Unfortunately, many underlying processes, such as granulation, waves, flows, and jets, are not reproduced by 1D SE models as they are obtained using the hydrostatic equilibrium and plane-parallel geometry approximation (Rutten 2002). These processes are better represented by computationally much more expensive 3D-MHD models, which also have limitations mentioned in the first paragraph of this section. This may justify an employment of 1D modeling particularly when the challenging off-limb viewing geometry is considered.

It has been shown that specific monochromatic intensities of some chromospheric lines sample the TM layer and can be used to study the location and properties of this layer. For example, the K_1 feature of the Ca II K line can map the TM in the solar and stellar atmospheres (e.g., Shine et al. 1975; Ayres & Linsky 1976; Avrett 1985; Mauas 2000). The most cited paper on SE non-LTE models by Vernazza et al. (1981) places the TM with the local temperature of ∼4200 K about 500 km above the visible solar surface, corresponding to the optical depth unity at 5000 Å. Since then, the temperature and the location of the TM have been the subject of intensive discussion. Fontenla et al. (2007) list previous papers preferring warmer or cooler TM models, divided further into single component or bifurcated, and present a single-component model, which matches several apparently contradictory observations. For example, SE models of sunspot by Maltby et al. (1986) place TM at a height of around 300–550 km. Analyzing the flare spectra of Ca II H and K lines, Machado & Linsky (1975) showed that the TM in flares is hotter and formed deeper in the atmosphere than in quiet-Sun models. Similar results have been found by Kuridze et al. (2017), who constructed SE model of C-class flare employing high-resolution SST observations of the Ca II 8542 Å and non-LTE inversions.

Spectral diagnostics of thermal conditions near and above the TM utilizes the strong vibration-rotation lines of carbon monoxide (CO) at 4.6 μm. Remarkably, the solar CO spectra suggest the coexistence of a cool (less than 4000 K) component of the solar chromosphere with a hot, bright gas at 6000–7000 K. Large horizontal velocities are observed, implying that the cool component is sustained by the supersonic adiabatic expansion of upwelling gas in overshooting granules (Solanki et al. 1994). This motivated the introduction of the concepts of thermal bifurcation in the solar outer atmosphere (Ayres 1981) and the so-called COmosphere, a term coined by G. Wiedemann (Wiedemann et al. 1994; Ayres 2002). This zone probably consists of patchy clouds of cool gas, seen readily in off-limb emissions of CO lines, threaded by hot gas entrained in long-lived magnetic filaments as well as transient shock fronts (Ayres 2003, 2010). The COmosphere was not anticipated in classical 1D models of the solar outer atmosphere but is quite at home in the contemporary 3D highly dynamic view (Wedemeyer et al. 2004).

The 3D R-MHD modeling confirms that the lower solar atmosphere has a much more complex temperature structure where the location of the TM is not well defined (Bjørgen et al. 2019, Figures 12–15). However, the spatially averaged temperature structure of these models is still characterized by a single well-defined TM layer that can be assumed as a boundary between the photosphere and chromosphere. This raises the question of whether the TM is a local, dynamic plasma parameter rather than a homogeneous global property of the atmosphere. Surprisingly, Wedemeyer et al. (2004) concluded that the TM and the upward-oriented temperature gradient derived from semiempirical models might be illusive in the sense that they do not really mean a rise of the average gas temperature with height.

One of the key aspects that controls the physical condition in which the emergent intensity forms in the lower atmosphere is the radiative coupling between the plasma and the underlying radiation. The chromosphere is a highly non-LTE environment where radiation is weakly coupled to the local plasma condition. Furthermore, the lower atmosphere is highly structured by various processes (convection, jets, magnetic flux tubes, oscillations, waves), which appear as large- and small-scale perturbations of the plasma. The response of the the inhomogeneous, dynamic plasma to the underlying radiation defines the complex temperature structure of the atmosphere, which is manifested in high-resolution, state-of-the-art models and observations. Therefore, the transitional layer between the photosphere and chromosphere can be introduced in terms of this interaction rather than the simple position of the TM. The chromosphere can be defined as a region where hydrogen stays predominantly neutral as a result of this complex interaction (Carlsson 2007).

Chromospheric off-limb observations offer a new view into the problem of the TM in association with an off-limb feature called the intensity dark gap or the intensity dip introduced in Judge & Carlsson (2010). The wide-band off-limb filtergrams in the Hα center by Loughhead (1969), Nikolsky (1970), and Alissandrakis & Macris (1971) revealed the dark gap, referred to as the dark stripe and the dark band in the two latter papers, crowned with a shell of enhanced chromospheric emission. Loughhead (1969) suggested that the observed dark gap can be associated with the TM region of the solar atmosphere (Alissandrakis & Macris 1971).

Judge & Carlsson (2010) analyzed broadband Ca II H filtergrams of limb spicules obtained by Hinode's Solar Optical Telescope and pointed to a dip in the synthetic intensities, which is not in qualitative disagreement with the dip in the Hα line-center intensities discovered by Loughhead (1969). Because the relevant formulations by Judge & Carlsson (2010, Section 4.2) are very apt in this context, we quote them directly: "The cores of Hα and neutral helium lines routinely show a dip in intensity surrounded by a shell of emission (e.g., White 1963; Loughhead 1969; Pope & Schoolman 1975). However, dips seen in visible lines of hydrogen and helium may result more from the well-known lack of opacity in the low to mid chromosphere and extra opacity due to fibrils which appear to overarch the stratified chromosphere. Resolving the issue would require detailed calculations of Hα and He lines with models taking into account the fibril structure and excitation mechanisms populating these excited atomic levels." However, a few lines further they emphasize: "Importantly, we also note that our calculations never remove the off-limb dip entirely … yet at least some of the Hinode BFI images appear to show no hint of a dip."

The mentioned helium dip is well visible in the narrowband filtergram in the He I D3 line center by Libbrecht (2016, p. 60, Figure 4.5). The formation of the midchromospheric Hα opacity gap is shown in Leenaarts et al. (2012). Recently, Pazira et al. (2017) detected the dark gap in the O I 7772 Å line center with the narrowband observations obtained with the

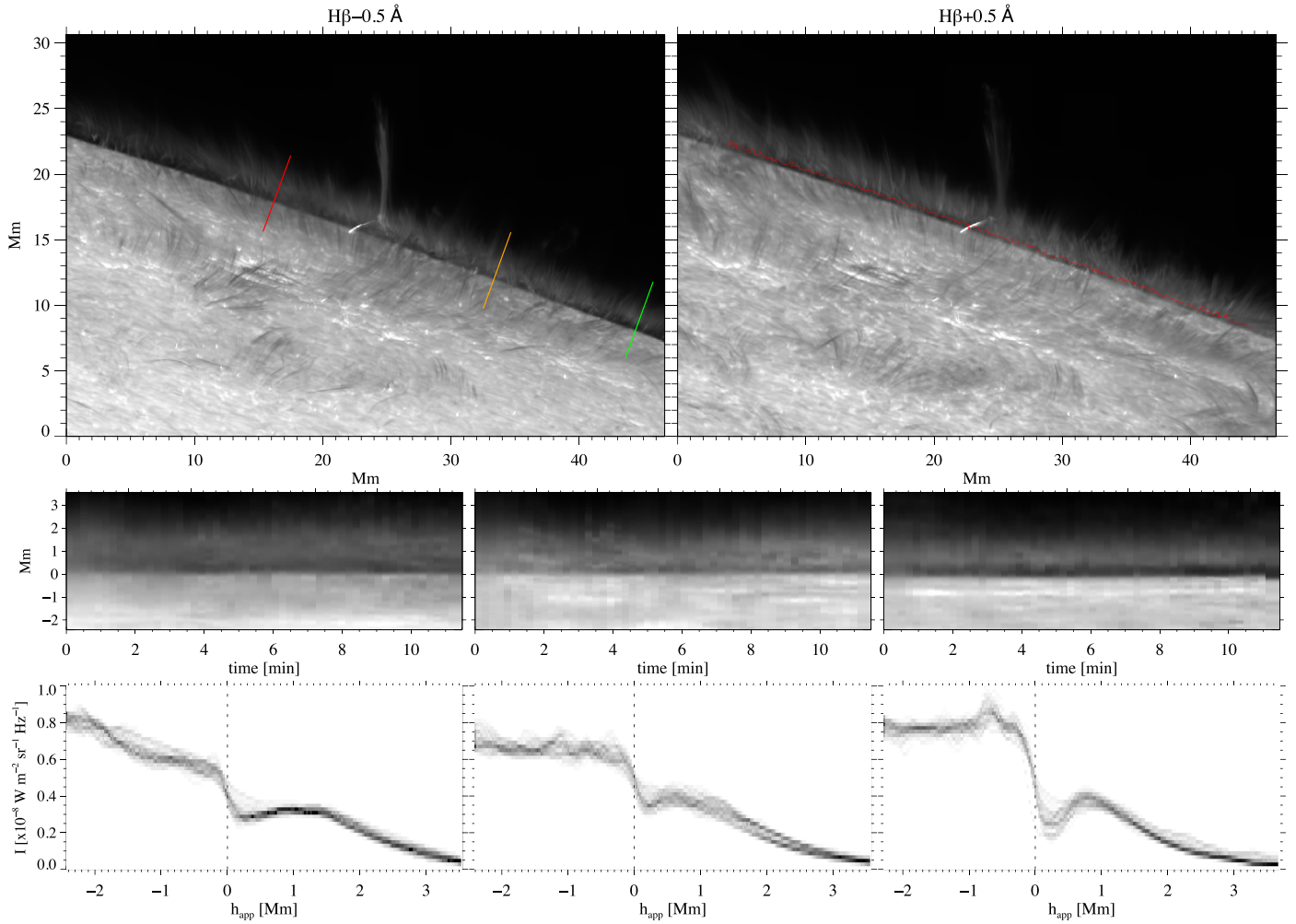

Figure 1. Top: CHROMIS Hβ wing images at $\Delta\lambda = -0.5$ Å (left) and $+0.5$ Å (right). The red contour in the top-right panel follows the locations of minimum intensity in the dark gap. Middle: time–distance diagrams of intensities extracted along the dashes in the top-left panel. Bottom: superimposition of the extracted intensities at individual times shown in the middle panels. The zero apparent height of the photospheric limb corresponds to the position of the inflection point (the vertical dashed line) of the radial intensity gradients along the dashes pertinent to the Hβ far wing image at $\Delta\lambda = -1.2$ Å.

CRisp Imaging SpectroPolarimeter (CRISP) on the Swedish Solar Telescope (SST). In concert with Judge & Carlsson (2010), they concluded that the dark gap is produced by height variations of the line opacity and corresponds to the TM layer.

This paper continues the previous detection and modeling of the dark gap but using high-resolution imaging spectroscopy data of the solar limb in the Hβ and Ca II 8542 Å lines, analyzing them with the radiative transfer code RH by Uitenbroek (2001) in one-dimensional spherical geometry. We study the emergent intensities from different heights with respect to the photospheric limb and detect the dark gap between the photosphere and chromosphere in Hβ line-wing images. We analyze the line contribution functions of the synthetic spectra and their components to interpret the spectral characteristics of the observed off-limb emissions, including the formation of the dark gap.

2. Observations and Data Reduction

2.1. Observational Setup

We observed the western limb of the Sun on 2018 June 22 between 08:20 and 08:43 UT near the active region NOAA 12714 (Figure 1). The observations were made with the CRISP (Scharmer 2006; Scharmer et al. 2008) and the CHROMospheric Imaging Spectrometer (CHROMIS) (Löfdahl et al. 2021) instruments, both based on dual Fabry–Pérot interferometers mounted on the SST (Scharmer et al. 2003a, 2003b). The CHROMIS observations include narrowband spectral imaging in the Hβ spectral line. The line profile scan consists of 21 profile samples ranging from -1.2 Å to $+1.2$ Å at positions ±1.2, ±1.0, ±0.8, ±0.7, ±0.6, ±0.5, ±0.4, ±0.3, ±0.2, ±0.1, and 0.0 Å from the line center. CHROMIS data are processed using the CHROMISRED reduction pipeline (currently referred to as SSTRED), which includes MOMFBD image restoration and absolute intensity calibration (Löfdahl et al. 2021). The CRISP data comprise narrowband imaging spectropolarimetry in the Ca II 8542 Å line profile sampled from -1.75 Å to $+1.75$ Å in 21 line positions, ±1.75, ±0.945, ±0.735, ±0.595, ±0.455, ±0.35, ±0.28, ±0.21, ±0.14, ±0.07, and 0.0 Å from the line center (hereafter, unless specified otherwise, when referring to the Ca II line we mean the Ca II 8542 Å line). The acquisition time of each spectral scan of the Ca II line was 16 s but the cadence of the time series was 33 s due to interleaved spectropolarimetric scans in the Fe I 6302 Å line. More details on the observations and data can be found in Kuridze et al. (2021). In the following, we employ

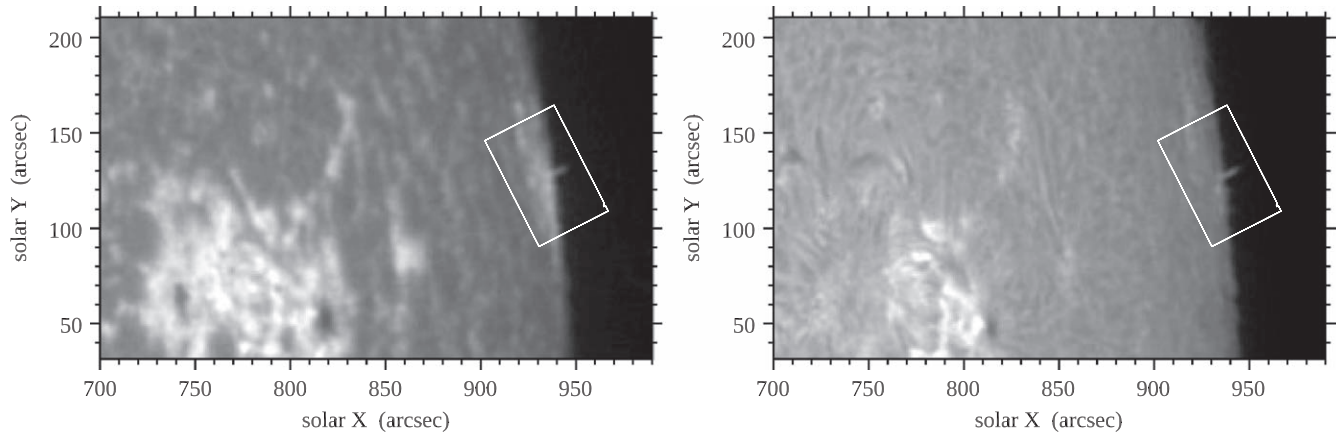

Figure 2. ChroTel Ca II K (left) and Hα (right) images, taken on 2018 June 22 at 08:34 UT, when the remnants of the decaying AR NOAA 12714 at the limb display the jet at (x, y) = (940″, 130″), which corresponds to the long spicule in the top panels of Figure 1 and in the left panel of Figure 4.

data from the 13 minute subinterval of the observational run lasting about 23 minutes.

Context images of the observed region in the Ca II K and Hα filtergrams (Figure 2) are provided by the 10 cm robotic Chromospheric Telescope (ChroTel; Kentischer et al. 2008; Bethge et al. 2011), located at the Observatorio del Teide on Tenerife. ChroTel is a multiwavelength imaging telescope for full-disk synoptic observations of the solar chromosphere in the Ca II K, Hα, and He I 10830 Å lines.

2.2. Radiometric Calibration and Convolution

The comparison of SST data with outputs of radiative transfer computations requires careful intensity calibration of the former and convolution of the latter with the transmission profiles of the SST instruments provided by J. de la Cruz Rodríguez (2017, private communication) and M. Löfdahl (2019, private communication). Here we use the same CRISP data as in the paper by Kuridze et al. (2021), and its Section 2.2, "Data Radiometric Calibration," is also valid for this work. The processing pipeline yields the CHROMIS data implicitly calibrated in disk-center absolute intensity units using the Hamburg disk-center spectral atlas as a reference (Neckel 1999), disregarding the actual position angle of the CHROMIS science data (Löfdahl et al. 2021, Section 4.4). Therefore, we perform a recalibration of the CHROMIS data following the same procedure as for the CRISP data but taking the Hβ profiles from David (1961) as a calibration reference and the CHROMIS transmission profile provided by M. Löfdahl (2019, private communication). The resulting intensities expressed relative to the quiet-Sun continuum intensity at the disk center are converted to the absolute intensities in the radiometric units W m^{-2} sr^{-1} Hz^{-1} by the disk-center absolute continuum intensity taken from Cox (2000).

3. Analyses and Results

3.1. Appearance of the Hβ Dark Gap

The top panels of Figure 1 show the western limb in the Hβ line-wing images at $\Delta\lambda = \pm 0.5$ Å taken on 2018 June 22 at 08:34:24 UT. The SE model of the spicule in the center of the field of view (FoV) is presented in Kuridze et al. (2021). This work is aimed at the off-limb emissions from the edge of photosphere up to the chromosphere. Both Hβ wing images suggest the presence of a dark gap that closely follows the limb below the chromospheric canopy and the forest of type II spicules. To investigate the location of the dark gap, the intensities at different time moments are extracted along the three radial dashes of length 6 Mm shown in the top-left panel of Figure 1. The length of these dashes is chosen to cross the limb, the dark gap, and the off-limb chromosphere at different parts of the FoV. The time–distance diagrams along each dash (middle panels of Figure 1), and density diagrams produced by superimposition of extracted intensities at different time moments (bottom panels of Figure 1) clearly confirm the existence of a dark gap at the selected portions of the FoV over most of the 13 minute time span.

We define the observable photospheric limb in the Hβ imagery (hereafter the apparent limb) as the time-averaged positions of inflection points of the steepest intensity gradient along the dashes in the Hβ far wing image at $\Delta\lambda = -1.2$ Å (not shown). The position of the apparent limb defines the zero-point of the spatial scales at x-axes in the bottom panels of Figure 1. We will refer to the spatial scale as the apparent height denoted as $h_{\rm app}$. However, the position of the observable photospheric limb slightly varies, possibly due to small-scale photospheric inhomogeneities producing local Wilson depressions. Therefore, the apparent height of the dark gap also slightly varies along the observable photospheric limb. It is shown in the top-right panel of Figure 1 in which the red contour follows the positions of the dark-gap intensity minima yielding the average apparent height of 0.265 ± 0.055 Mm. We take this value as the height of the dark gap above the apparent limb.

We note that the apparent limb is uplifted by about 0.35 Mm above the level with the optical depth unity at 5000 Å viewed at the disk center. More details on the subject can be found in Athay (1976, pp. 8–9, 279–280) and Lites (1983, Table 1). This offset is due to an increase of distance corresponding to optical depth unity at 5000 Å when moving the line of sight (LoS) from the disk center ($\mu = 1$) to limb ($\mu = 0$).

Examples of the observed monochromatic intensities along the green dash are shown in the bottom-left panel of Figure 3. Here we introduce the reference height $h_{\rm ref}$ shifted with respect to $h_{\rm app}$ as $h_{\rm ref} = h_{\rm app} + 0.35$ Mm. It will be useful for later comparisons with the synthetic intensities computed by the RH code, which will refer to the base of the photosphere ($h_{\rm ref} = 0$ in the bottom-middle and right panels of Figure 3) with the optical

Table 1
Parameters of Prominent Chromospheric Lines

Atom/Ion	λ (Å)	$E_{\rm low}$ (eV)	$E_{\rm low}/k_{\rm B}T_{\rm e}$ [a]
He I D3	5876	21.0	34.8
He I	10830	19.8	32.8
Hα	6563	10.2	16.9
Hβ	4861	10.2	16.9
O I	7772	9.1	15.1
Ca II	8542	1.7	2.8
Ca II K	3934	0.0	0.0
Ca II H	3968	0.0	0.0

Note.
[a] Computed for a typical chromospheric electron temperature $T_{\rm e} \sim 7000$ K.

depth unity at 5000 Å. Now, the bottom-left panel of Figure 3 shows the dark gap at $\Delta\lambda = -0.5$ Å at $h_{\rm ref} \sim 0.6$ Mm compared to $h_{\rm app} \sim 0.265$ Mm in the bottom panels of Figure 1. Remarkably, the Hβ line-core intensity lacks any signature of a dark gap compared to the previous Hα, He I D3, and O I 7772 Å detection referred to in Section 1. The top-left panel of Figure 3 shows the Hβ line profiles at the dark gap at 0.6 Mm and at the point of the maximum off-limb emission (hereafter MOLE in the context of observed and synthetic intensities) outside the dark gap where the observed off-limb emission has its local maximum at the height of 1 Mm. For example, the contrast of the dark gap is apparent by comparing the profile intensities at, e.g., $\Delta\lambda = \pm 0.5$ Å. Generally, the Hβ wing intensities of the dark-gap profile at 0.6 Mm are reduced over the wavelength spans $(-0.9, -0.3)$ Å and (0.4, 1.1) Å compared to the MOLE profile. The Hβ reversed core in the dark gap is very close to the MOLE profile.

The left panel of Figure 4 shows the Ca II blue wing image at the wavelength position $\Delta\lambda = -0.945$ Å from the line center taken on 2018 June 22 at 08:34:27 UT at the western limb. The middle panel shows the monochromatic intensities extracted along the red dash in the left panel. The image and intensity extractions at all wavelength positions across the Ca II line scan lack any trace of a dark gap. Here the observable photospheric limb is also defined by the position of the inflection point of the intensity gradient along the red dash in the Ca II far wing image at $\Delta\lambda = -1.75$ Å (not shown). The position shifted about 0.35 Mm defines the height h used at x-axes in the middle and right panels. Here we omit the adjective "reference" and the subscript "ref" to distinguish h from its Hβ and RH counterpart $h_{\rm ref}$. This is because the end wavelength settings of the Ca II scans at $\Delta\lambda = -1.75$ Å do not reach yet a true photospheric continuum, thus introducing an unknown but likely small offset between the h and $h_{\rm ref}$ scales. Remarkably, the middle panel of Figure 4 clearly shows a small intensity enhancement at $\Delta\lambda = -0.945$ Å over the height span from 0.1 to 0.25 Mm. Such enhanced off-limb intensities are observed within the wavelength spans $(-0.945, -0.6)$ Å and (0.6, 0.945) Å of the Ca II profile.

4. RH Code and Viewing Geometry

To interpret the observational characteristics of the off-limb Hβ and Ca II line emissions, we generated synthetic line profiles with the radiative transfer code RH by Uitenbroek (2001). RH can calculate spectral line profiles for a model atmosphere by solving the equations of statistical equilibrium and radiative transfer under non-LTE conditions. We utilized the one-dimensional spherical version of the RH code. Spherical geometry takes into account the tangential variation of physical parameters along the LoS including optical depth, which is the main quantity for radiative transfer calculations. This makes spherical RH the most appropriate choice for calculations of off-limb emissions.

To synthesize the line profiles, we chose the SE model of a bright area of the network FAL-F (Fontenla et al. 1993) extending about 2 Mm from the base of the photosphere to the top of the chromosphere. This choice was motivated by the assumption that the formation of the Hβ and Ca II lines in the dark gap is affected by the remnants of the decaying AR NOAA 12714 seen at the limb in the context of Ca II K and Hα images (Figure 2) taken by the ChroTel.

We used the models of hydrogen and singly ionized calcium atoms with the five bound levels plus continuum with complete frequency redistribution for the former (apart from the Lyα and Lyβ transitions, which were calculated in partial frequency redistribution (PRD)) and the PRD with the cross-redistribution for Raman scattering for the latter.

The RH computes emergent intensities at the top of the model atmosphere at 81 predefined direction cosines μ_i, indexed as $i = 1,...81$, from the disk center at $\mu_{81} = 1$ to the top of the chromosphere at $\mu_1 \sim 0$ assumed at the height $H = 2$ Mm above the base of the photosphere. Figure 5 shows a sketch of the viewing geometry of different LoS rays passing closer to (μ_i, h_i) or farther from (μ_j, h_j), the base of the photosphere corresponding to the reference height $h_{\rm ref} = 0$. Note that $\mu_i > \mu_j$ and $h_i < h_j$ in this sketch. Therefore, in our RH calculations, $\mu_1 \sim 0$ and $\mu_{67} \sim 0.078$ correspond to the tangential rays touching the top of the chromosphere and the base of the photosphere, respectively. Thus, the rays along μ_i with $0 < i < 67$ represent the emissions emerging from different heights between $h_{\rm ref} \sim 0$ to ~ 2 Mm (Figure 5) in the direction of the LoS. The conversion formula between the predefined direction cosines μ_i and the corresponding reference heights $h_{\rm ref,i}$ reads

$$h_{\rm ref,i} = (\mathcal{R}_\odot^{\rm N} + H)\sqrt{1 - \mu_i^2} - \mathcal{R}_\odot^{\rm N}, \quad (1)$$

where $\mathcal{R}_\odot^{\rm N}$ is the nominal solar radius.

4.1. Synthetic Hβ and Ca II 8542 Å Line Profiles

The synthetic emergent monochromatic intensities of the Hβ line along off-limb LoS rays as a function of the reference height $h_{\rm ref}$ (Section 3.1) are presented in the bottom-middle and right panels of Figure 3 for the three spectral positions. The middle panels show the intensities for the FAL-F atmosphere with a standard microturbulence velocity input. While an intensity dip (i.e., the dark gap) is detected at the height of 0.6 Mm at the blue wing spectral position of $\Delta\lambda = -0.5$ Å, there are no intensity variations in the line core (bottom-middle panel of Figure 3). The top middle panel of Figure 3 shows the synthetic Hβ dark gap and MOLE profiles at $h_{\rm ref} \sim 0.6$ Mm and 0.9 Mm, respectively. It demonstrates that the wing intensities of the MOLE profile are only slightly enhanced over the wavelength spans $|\Delta\lambda| \in (0.35, 0.55)$ Å compared to the Hβ line-wing intensities at the height of 0.6 Mm. It produces a synthetic contrast observable as the dark gap.

We have also synthesized line profiles for the FAL-F model with increased microturbulence in the chromosphere (right

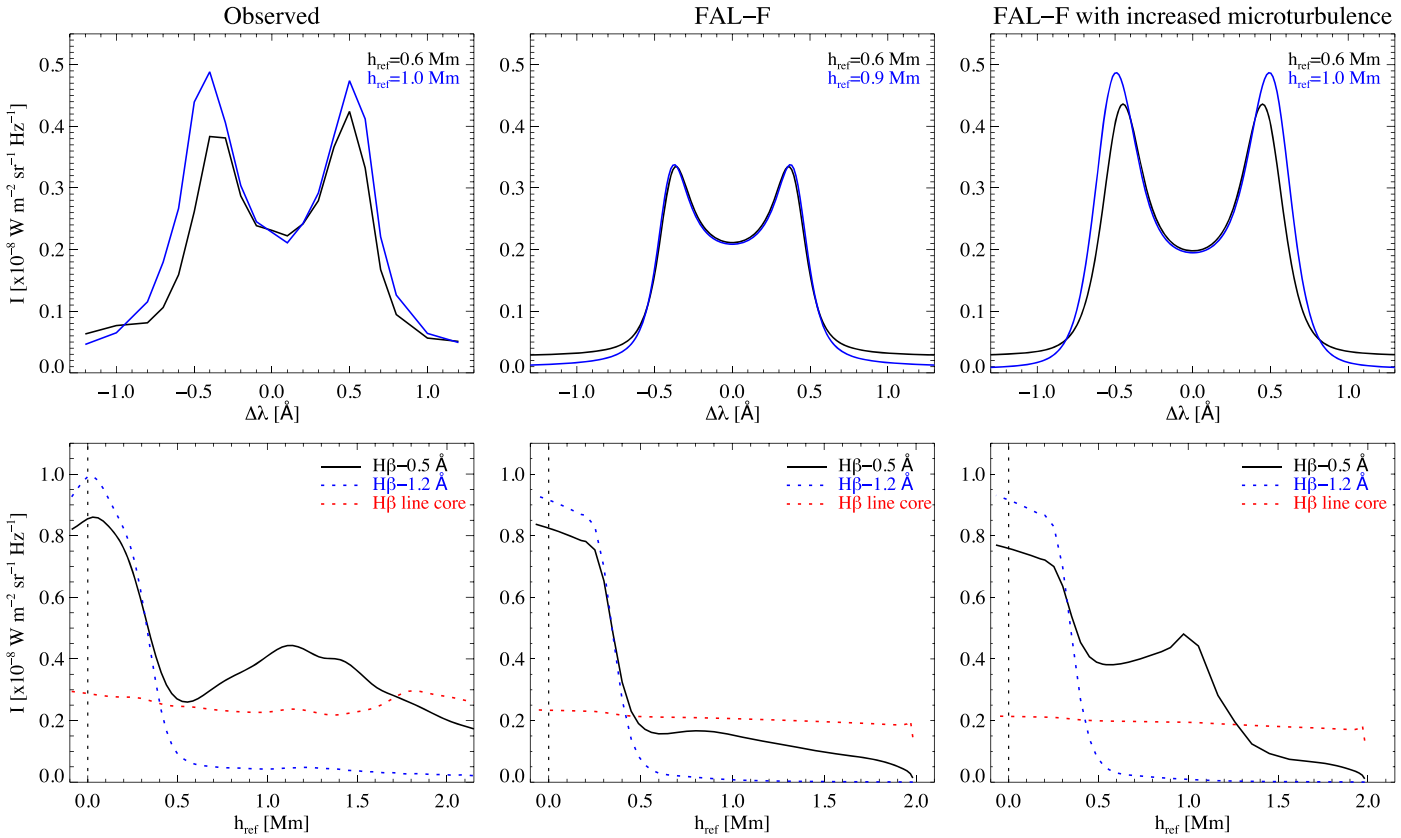

Figure 3. Top: observed (left) and synthetic (middle and right) Hβ line profiles in the dark gap at $h_{\rm ref} \sim 0.6$ Mm (black) and at the maximum of the chromospheric emission at $h_{\rm ref} \sim 1$ Mm (blue). Bottom: observed (left) and synthetic (middle and right) monochromatic intensities at the indicated wavelength separations from the Hβ line center. The left panels pertain to the green dash in the top-left panel of Figure 1. The middle and right panels display the profiles for standard and increased microturbulence in the FAL-F model, respectively.

panels of Figure 3). In FAL-F, at a height range covering ∼0.8–1.4 Mm, $v_{\rm mic}$ varies between ∼1 and 5 km s^{-1}. We took $v_{\rm mic}(h_{\rm ref} = 0.8\text{–}1.5$ Mm) ∼4–13 km s^{-1} in the FAL-F model. Here we use quite different viewing angles (off limb) than in SE models like FAL (on disk), and we assume that the projected LoS velocities have a larger scatter. The resulting line profile and intensity as a function of height are presented in the right panels of Figure 3. The increased microturbulence produces broader line profiles and higher contrast between the dark-gap and MOLE line-wing intensities. Furthermore, a gap is formed over a wider wavelength range extending toward the outer wings at $|\Delta\lambda| \in (0.4,\ 0.85)$ Å (top-right panel of Figure 3).

In contrast to Hβ, the synthetic monochromatic emergent intensities in the Ca II line wings (right panel of Figure 4) along off-limb LoS rays do not show the dark gap but the intensity enhancements at $h \sim 0.6$ Mm within the wavelength spans of $(-0.3,\ -0.6)$ Å and $(0.3,\ 0.6)$ Å. We note that the results presented in the middle and right panels of Figure 3 and also in the right panel of Figure 4 are convolved with the instrumental characteristics of the CHROMIS and CRISP instruments, respectively.

Finally, the results (synthetic profiles, appearance of the dark gap) obtained through RH calculations with the FAL-F model atmosphere are very similar to those by the FAL-C model (an average region of the quiet Sun). However, due to the better match between the absolute observed and synthetic intensities (compare the left and right panels in Figure 3), we give priority to the FAL-F model in this work. Our selection is also justified with context images of the larger FoV, confirming that observed limb contains a chromospheric bright network, which makes FAL-F the more appropriate model for the observed data (Figure 2.)

4.2. Understanding the Dark-gap Formation

To understand the off-limb Hβ and Ca II emissions, we examine their intensity contribution functions C_I at selected gap-pertinent wavelengths as a function of distance along off-limb LoS rays. The emergent intensity I_ν can be expressed in terms of the contribution function (Carlsson & Stein 1994),

$$I_\nu = \int_{\rm LoS} C_I\, dl = \int_{\rm LoS} S_\nu\, \chi_\nu \exp(-\tau_\nu) dl, \qquad (2)$$

where S_ν is the source function at the frequency ν, χ_ν is the opacity, τ_ν is the optical depth, and l is the geometrical distance along the LoS. Its zero reference point corresponds to the cross point of the viewing LoS ray with the normal to both the photospheric surface and the ray (Figure 5). The positive l values increase toward the observer.

Figure 6 shows the intensity contribution function C_I of the FAL-F atmosphere with a standard microturbulence input for the Hβ blue wing at $\Delta\lambda = -0.44$ Å (bottom-right panel) and its components at the dark gap (black curves) and at the point of MOLE (blue curves). To facilitate reading, the panel references omit Figure 6 in this paragraph. For the ray passing through the dark gap, the line wings have the lowest opacity χ and emissivity η near the limb at $l = 0$ Mm (black solid and black

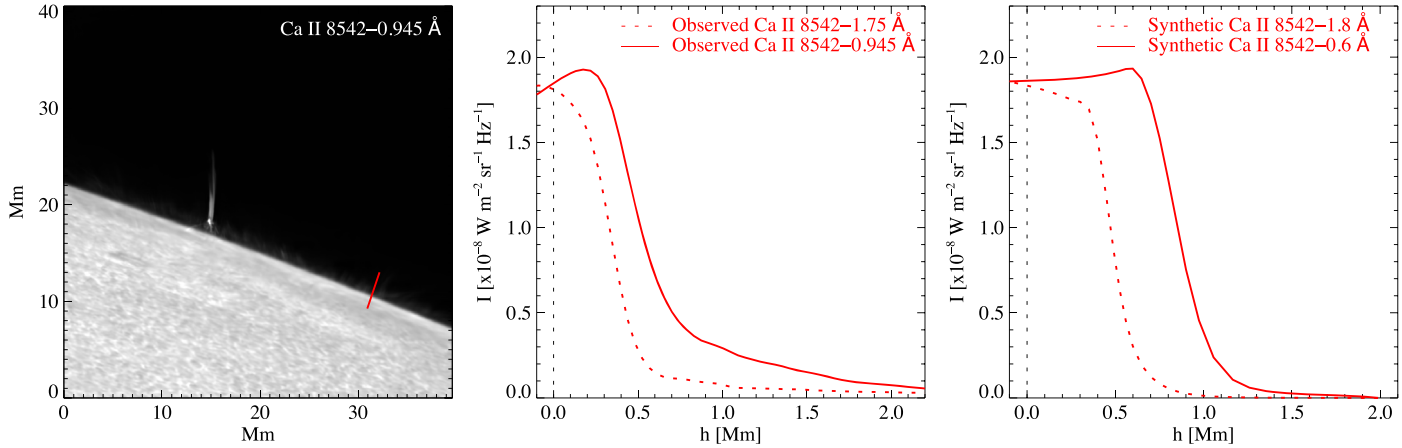

Figure 4. CRISP Ca II 8542 Å blue wing image at $\Delta\lambda = -0.945$ Å (left). Observed monochromatic intensities along the red dash in the left panel (middle) and synthetic intensities (right).

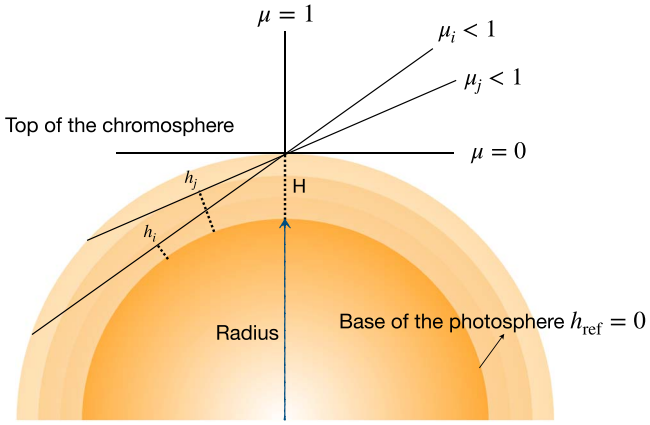

Figure 5. Sketch of the off-limb geometry showing the LoS rays passing at different heights h_i and h_j above the base of the photosphere. The RH code computes emergent intensities at the top of the model atmosphere. As a result, $\mu = 0$ corresponds to the emergent intensity at the height $H = 2$ Mm above the base of the photosphere at $h_{\rm ref} = 0$.

dashed curves, respectively, in the top-left panel). The optical depth unity is reached at the farthest point of the dark-gap atmosphere at $l \sim -40$ Mm (black curve in the bottom-left panel). However, due to the low emissivity η of the dark-gap atmosphere (black dashed in the top-left panel), there is very little contribution to the emergent intensity over the LoS span $(-10, 10)$ Mm (black curve in the bottom-right panel). The ray passing through the point of MOLE at 0.9 Mm is characterized by a slightly higher optical depth τ of about 1.2 (blue curve in the bottom-left panel). However, a high emissivity η at this point over the LoS span (–10, 10) Mm (blue dashed in the top-left panel) yields a higher emergent intensity than in the dark gap (blue curve in the bottom-right panel).

Figure 7 shows the intensity contribution function C_I for the Ca II blue wing at $\Delta\lambda = -0.6$ Å (bottom-right panel) and its components at the point of MOLE at 0.6 Mm (black curves; see also the right panel of Figure 4), coinciding with the height of the Hβ dark gap, and at the height of 0.45 Mm (blue curves) selected for comparison. C_I components indicate that the ray passing through the atmosphere at ~0.6 Mm experiences low opacity χ, low emissivity η, and optical depth τ (top-left and bottom-left panels of Figure 7), resulting in optically thin emission. At ~0.45 Mm, the rays originate in an optically thicker environment at $\tau \sim 7$, attenuating the emissivity through the factor $\exp(-\tau)$. As a result, the off-limb emission at the Ca II line wing, emerging at ~0.6 Mm, has a higher intensity than at ~0.45 Mm.

4.3. Understanding the Dark-gap Visibility Didactically

In Section 4.2 we attempted to render a rigorous explanation of the dark-gap visibility in the context of the TM region. Here we offer a more straightforward account for why the dark gap is visible in Hβ and other chromospheric lines, listed in Section 1, but not in Ca II.

The line opacity is proportional to the fraction of atoms (or ions) excited to the nth level, which scales with the Boltzmann factor as const $\times\, g_{\rm low}\, e^{-E_{\rm low}/k_B T_e}$, where $g_{\rm low}$ and $E_{\rm low}$ are the statistical weight and energy of the lower level of transition, respectively, k_B is the Boltzmann constant, and T_e is the electron temperature (Gray 2008). Table 1 shows the lower-level energies and the exponents of the Boltzmann factor for $T_e \sim 7000$ K for prominent chromospheric spectral lines. The lines with $E_{\rm low} \gg 1$ eV have a high Boltzmann factor exponent, suggesting they should have low opacities in the chromosphere. This explains why the dark gap is well visible in the He I, Balmer, and O I lines but hardly or not at all in the Ca II line.

However, the Ca II H and K lines throw uncertainty on the proposed scenario which suggests that the presence or absence of a dark gap is controlled by the $E_{\rm low}$ of transition. The model calculations of Ca II H by Judge & Carlsson (2010, Figure 5) never remove the off-limb dip entirely, which should not appear at all like in our observations and calculations of Ca II 8542 Å.

5. Discussion

The wing detection of the dark gap and its absence in the Hβ core is particularly significant in the context of a previous gap detection in Hα, He I D3, and O I 7772 Å reviewed in Section 1. The gap detection in Hα pertained to wide-band observations blending the line center and wing intensities. The high inherent opaqueness of the chromosphere in the Hα center enhanced further by the spicules and the chromospheric canopy prevents observing the dark gap in the Hα center. We consider the past Hα detection in fact for wing detection in the regime of low Hα optical thickness outside the thick opacity wall due to the spicules and the canopy. On the other hand, the recent narrowband gap detection by the SST/CRISP in the He I D3

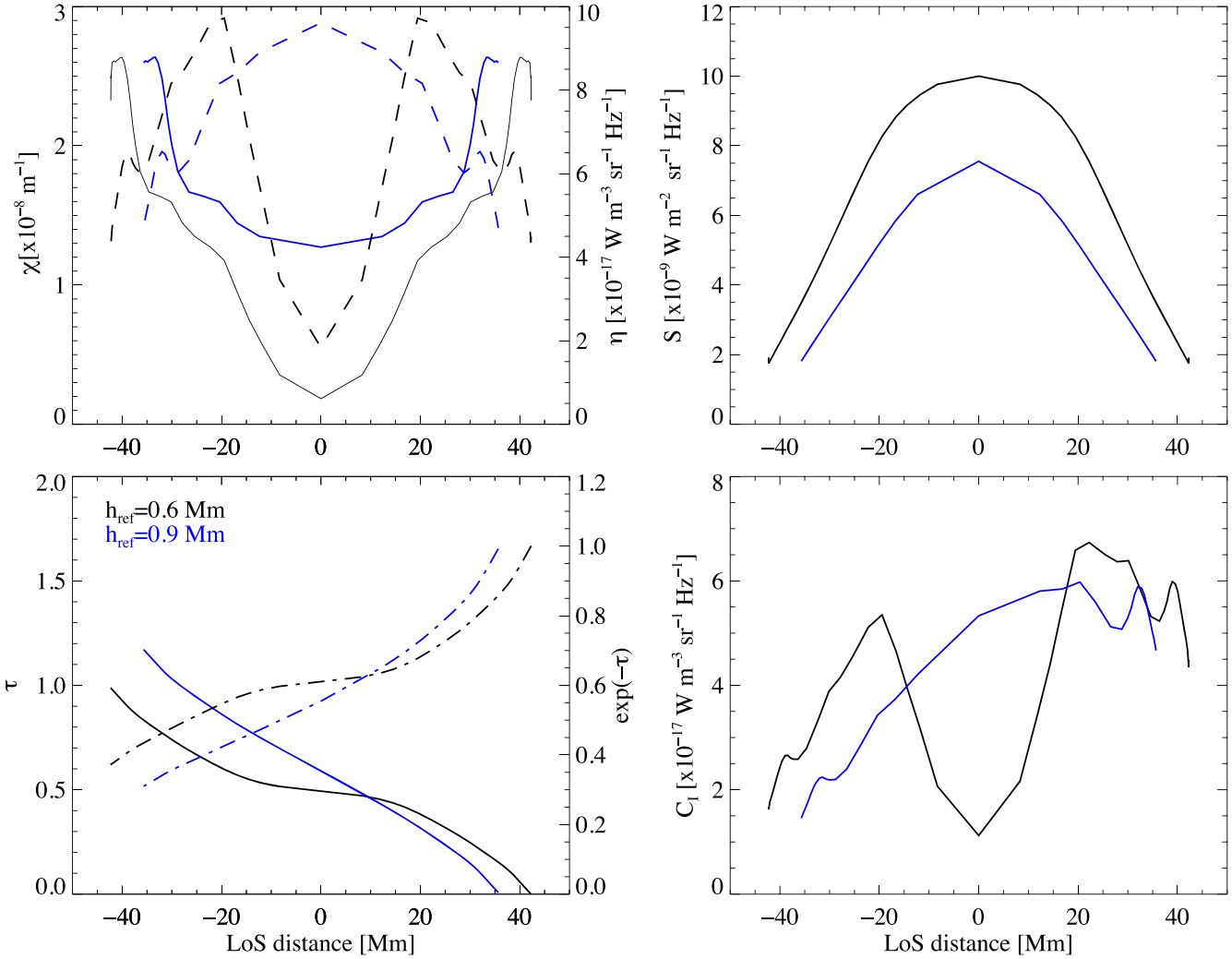

Figure 6. Formation characteristics of the Hβ blue wing intensities at $\Delta\lambda = -0.44$ Å shown along the LoS in the dark gap at the reference height $h_{\rm ref} \sim 0.6$ Mm (black) and at the maximum off-limb emissivity at 0.9 Mm (blue). Top left: opacity χ (left y-axis) and emissivity η (right y-axis) as the solid and dashed lines, respectively. Top right: the source function S. Bottom left: the optical depth τ (left y-axis) and the exponential $\exp(-\tau)$ (right y-axis) shown as the solid and dashed–dotted lines, respectively. Bottom right: the intensity contribution function C_I.

and O I 7772 Å centers give evidence of the low inherent optical thickness of the chromosphere (Pazira et al. 2017, τ in Figure 7), the spicules, and the canopy in these lines. We note that in Pazira et al. (2017) there is around a 170 km difference between the location of the dark gap in observed and synthetic O I 7772 Å line-core intensities (Pazira et al. 2017, Figure 6). For the Hβ analyzed in this work, both the observed and synthetic gaps, computed by the FAL-F and FAL-C models, are located at ∼0.6 Mm, suggesting that Hβ line-wing images could be a better tracer of the TM layer.

There are noticeable differences between the properties of the dark gap in the observations and the RH radiative transfer simulations. In particular, (i) the observed contrast of the dark gap with respect to the maximum off-limb emission is larger in observations than in the RH simulations (bottom panels in Figure 3); (ii) the observed Hβ profiles are broader and asymmetric compared to the synthetic profiles (top panels in Figure 3); (iii) a dark gap is seen along a wider spectral range in the observation covering around $|\Delta\lambda| \in (0.4, 1)$ Å, at the blue and red wings, whereas with standard FAL-F microturbulence velocities, a gap is only detected at $|\Delta\lambda| \in (0.35, 0.55)$ Å. We explain these differences as due to the absence of a realistic model of spicules and the chromospheric canopy in the RH simulations. Spicule emission contributes to the observed emergent intensities in the layers above the dark gap, thus enhancing the observed contrast. Spicule hydrogen profiles of the Balmer series are broad, with enhanced and asymmetric wings (Beckers 1972; Shoji et al. 2010). It likely makes the observed Hβ profiles broad and asymmetric as captured in our observations. To investigate the effect of extra broadening introduced by chromospheric dynamics such as spicules, flows, jets, and MHD waves, we performed a simple test using increased microturbulence in the FAL-F model at the heights of 0.8–1.5 Mm above the photosphere. The resulting profiles showing a broad line width and the presence of the dark gap at the outer wing positions at $|\Delta\lambda| \in (0.4, 0.85)$ Å are in good agreement with the observations (top-left and right panels of Figure 3).

The dark gap is absent in Ca II, both in observations and simulations (Figure 4). As discussed in Cauzzi et al. (2008), an opacity gap in the Ca II line wings is less prominent due to the much lower excitation energy of 1.7 eV of the D term of the Ca II infrared triplet compared to the excitation energy of hydrogen upper levels 10.2 eV (Table 1). Furthermore, the low

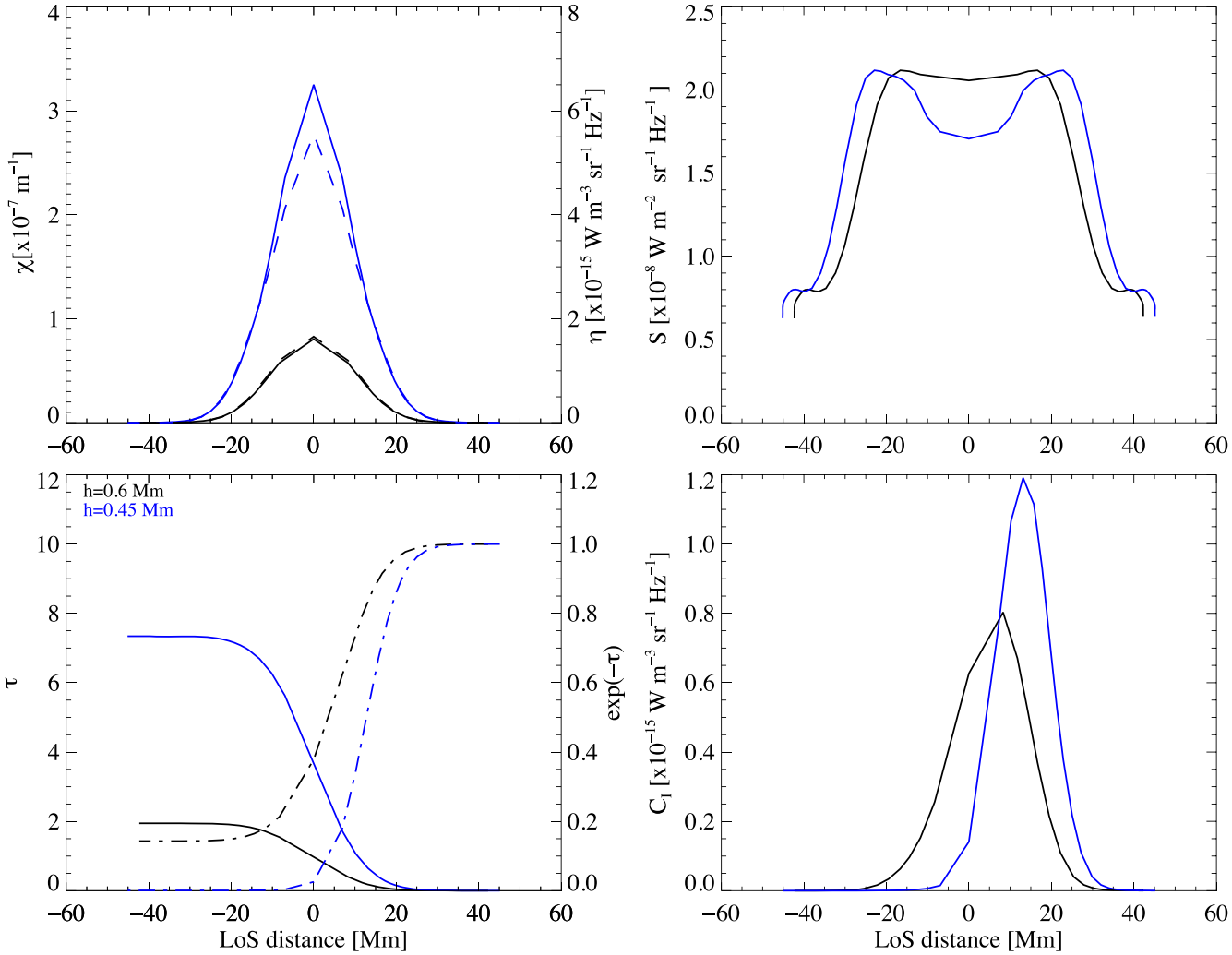

Figure 7. Formation characteristics of the Ca II 8542 Å blue wing intensities at $\Delta\lambda = -0.6$ Å shown along the LoS at the heights $h \sim 0.45$ Mm (blue) and 0.6 Mm (black). Panel descriptions are the same as in Figure 6.

optical depth of the Ca II line-wing emission produces higher off-limb synthetic emergent intensity at ∼0.6 Mm than at ∼0.45 Mm from the photospheric limb (Figures 4 and 7).

In the past, eclipse flash spectra provided a sound basis for determining physical conditions in the chromosphere (Athay et al. 1954; Judge et al. 2019). Out of the wealth of continuum and line spectral data presented therein, we concentrate further just on the Hβ data (Athay et al. 1954, Table 2). The Hβ flash spectra sampled the quiet-Sun chromosphere over heights from 530 km up to 6300 km above the photospheric limb, yielding 20 samples with a regular cadence of 0.4 s and a step size of 110 km in the lower chromosphere but increasing higher up. Notice the blue circles in Figure 8 comparing the wavelength- and area-integrated Hβ intensity E as a function of the height h above the photospheric limb derived from the SST/CHROMIS data (black) and the 1952 eclipse flash spectra shown also in Athay (1976, p. 177, Figure V–7.). Both gradient curves compare well in the low chromosphere up to $h \sim 2000$ km. Higher up, they bear on spicules as broadly discussed in Athay (1976). The SST curve indicates relatively brighter spicules than those captured by the eclipse flash spectrum. This is in full agreement with the results by Judge & Carlsson (2010, Figure 5) showing brighter spicules in the Ca II H images acquired in the polar coronal hole than those captured in the flash spectrum. It was shown in Athay (1976, Chapter II) that when even 0.1%–1% of the disk area is covered with spicule-like features, the effects on the limb are dramatic. It is entirely possible, and probable as well, that nearly all of the emission at the limb above heights of 1500 km arises in spicules covering less than 1% of the solar surface (Athay 1976, p. 305). These same spicules would have a quite negligible effect on much of the emission observed near the disk center (Judge et al. 2020). Assuming that the limb is completely covered by spicules at $h \sim 3000$ km and that at $h \sim 5000$ km the mean fraction of the limb covered by spicules is approximately 10%, Athay (1976, pp. 178–179) suggested that most of the decrease in Hβ brightness above 3000 km is due to the decreasing of the surface area of spicules. The plausibility of this suggestion is demonstrated in Figure VII–9 of Athay (1976, p. 305) showing the relative decrease in spicule numbers and the Hβ emission. Thus, the spicule number distribution falls off more slowly with height than does the Hβ emission (Athay 1976, p. 305). It follows that if the spicules are effectively thin and have outwardly decreasing material density, they can account for the observed Hβ line emission above a height of about 2500 km (Athay 1976, pp. 305–306, Figure VII–10).

Judge et al. (2020) examined possible candidates for the differences in central reversal (canter-to-peak ratio) between

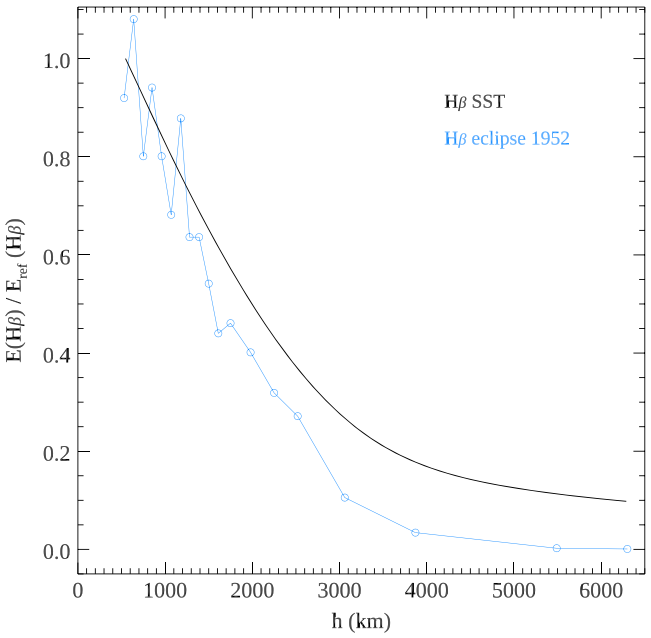

Figure 8. Relative Hβ height gradients, $E/E_{\rm ref}$. The wavelength- and area-integrated intensity E of the Hβ line as a function of the height above the photospheric limb h derived from the SST/CHROMIS spectral imaging at the limb on 2018 June 22 (black) and from the flash spectra (blue) obtained at the 1952 eclipse in Khartoum (Athay et al. 1954, Table 2). The SST intensities E are normalized with respect to the ad hoc reference intensity $E_{\rm ref}$ at $h = 530$ km. The eclipse intensities E are normalized with respect to the ad hoc reference value $E_{\rm ref}$ taken as an average of the intensities at the heights 530 km and 640 km.

the observed and synthetic chromospheric lines such as Lyα, Mg II h and k, Ca II H, and K. They analyzed disk profiles and concluded that micro and macroturbulence are not responsible for the observed discrepancies. They also admitted that the area coverage of spicules is too small to contribute significantly to the spatially averaged profiles (p. 4 therein, left column). However, as mentioned above, the effects of spicules at the limb are dramatic (Athay 1976, p. 305) as more spicules are expected to be aligned along the LoS. Our motivation for invoking enhanced microturbulence was sparked by the results presented in Tei et al. (2020) proving a profound effect of microturbulence on the Mg II h and k profiles of spicules computed by multislab non-LTE modeling. A question may arise whether macroturbulence may account for the dark gap as well. An effect of macroturbulence on a line profile is formally represented by a convolution affecting inevitably the whole line profile, including its core. However, as we show in Figures 1 and 3 the dark gap pertains only line wings and not the core. This excludes macroturbulence from any considerations and keeps microturbulence as a viable representation of the multitude of spicules at the limb in radiative transfer calculations by the spherical RH code.

6. Conclusions

We have analyzed high-resolution off-limb imaging spectroscopy in the Hβ and Ca II 8542 Å lines and compared them with radiative transfer computations. The Hβ line-wing images and intensity profiles of off-limb wing emissions show the dark gap at the height of about 0.265 Mm above the apparent photospheric limb (Figure 1) corresponding to the height of 0.6 Mm above the base of the photosphere (bottom-left panel of Figure 3). The gap disappears in the line-core and far wing images at $|\Delta\lambda| \gtrsim 1$ Å. Due to the spherical symmetry of the solar atmosphere, off-limb LoS chromospheric rays are passing through a very long ($\sim$100 Mm) geometrical path length covering very dynamic and nonhomogeneous chromospheric layers. Therefore, to understand the formation of the dark gap, radiative transfer calculations need to be performed for off-limb emissions in spherical geometry.

The synthetic Hβ profiles, computed by the RH code and the FAL-F model along off-limb LoS rays, confirm the existence of the dark gap at the height of 0.6 Mm, which is close to the temperature minimum region of the FAL-F atmosphere at about 0.525 Mm. The temperature of this region $\sim$4500 K is too low to populate the upper hydrogen levels, resulting in the opacity and emissivity gap (Cauzzi et al. 2008; Leenaarts et al. 2012). The off-limb LoS ray, passing at a height of $\sim$0.6 Mm, samples a large segment of the TM region with a meager population of relevant Hβ levels (Figure 5). The components of the intensity contribution function show that a strong opacity and emissivity gap in this layer makes the local plasma and the Hβ line-wing emission at, e.g., $|\Delta\lambda| \sim 0.4$–0.5 Å optically thin. On the contrary, the LoS ray at $\sim$0.9 Mm already samples layers with high Hβ wing emissivity above the TM region, thus producing an observable intensity contrast with the dark gap (top panels of Figure 1). We interpret the slight difference between the height of the TM at 0.525 Mm in the FAL-F model and the height of the dark gap at 0.6 Mm as a consequence of the location of the electron density minimum in FAL-F at 0.6 Mm. It shifts the opacity minimum and the dark gap above the TM layer.

The gap near the TM region was also detected in off-limb observations of the X8.2 class flare analyzed in Kuridze et al. (2019, 2020) (see Figure 2 in Kuridze et al. 2020). This indicates that Hβ off-limb observations can map the TM region under different atmospheric conditions.

The dark gap is absent in the Hβ line-core images (bottom-left panel of Figure 3). Its absence is due to a combination of opacity maximum in the line core at all off-limb positions, which is boosted by the high opaqueness of spicules and chromospheric canopy in the Hβ core hiding the dark gap beyond a thick opacity wall. The dark-gap absence in the Hβ core is reproduced in the RH radiative transfer calculations (bottom-middle and right panels in Figure 3) even without including a model of chromospheric canopy and spicules.

We demonstrate here that the off-limb emission in the Hβ wings shows a high-contrast gap that maps the TM region. Furthermore, our analyses showed that enhanced microturbulence in the chromosphere is required to reproduce the gap in the outer line-wing spectral positions. The nature of such an extra microturbulence can be various dynamical phenomena, such as spicules, MHD waves, jets, and shocks. The work opens a new window for studying the TM region by other lines of the Balmer series and with a more realistic chromospheric model atmosphere, which includes various dynamic phenomena relevant to the chromosphere. Trial Hα computations by the RH code and the FAL-C/F models (not shown here) also show the dark gap in the wings. However, Hα has a larger optical thickness than Hβ with a narrower line width, which makes the effect of spicules on the emergent intensities more important. These factors can make the Hβ line a better candidate for off-limb mapping of the TM region. The higher

Balmer lines (e.g., Hγ) can likely produce even better contrast between the TM layer and the upper layers.

D.K. acknowledges Science and Technology Facilities Council (STFC) grant ST/W000865/1, Leverhulme grant RPG2019-361 to Aberystwyth University and the excellent facilities and support of SuperComputing Wales. The Swedish 1-m Solar Telescope is operated on the island of La Palma by the Institute for Solar Physics of Stockholm University in the Spanish Observatorio del Roque de los Muchachos of the Instituto de Astrofísica de Canarias. J.K. acknowledges the project VEGA 2/0048/20. P.H. was supported by a grant of the Czech Funding Agency No. 19-09489S and by the program "Excellence Initiative—Research University" No. BPI-DUB.4610.96.2021.KG of the University of Wroclaw. R.O. acknowledges support from R+D+i project PID2020-112791GB-I00, financed by MCIN/AEI/10.13039/501100011033. ChroTel is operated by the Leibniz-Institute for Solar Physics in Freiburg, Germany, at the Spanish Observatorio del Teide, Tenerife, Canary Islands. The ChroTel filtergraph has been developed by the Leibniz-Institute for Solar Physics in cooperation with the High Altitude Observatory in Boulder, CO, USA. We would like to thank the anonymous referee for comments and suggestions that helped improve this paper.

Facility SST(CRISP, CHROMIS), Chromospheric Telescope (ChroTel).

Software: RH code (Uitenbroek 2001).

ORCID iDs

David Kuridze https://orcid.org/0000-0003-2760-2311
Petr Heinzel https://orcid.org/0000-0002-5778-2600
Július Koza https://orcid.org/0000-0002-7444-7046
Ramon Oliver https://orcid.org/0000-0003-4162-7240

References

Alissandrakis, C. E., & Macris, C. J. 1971, SoPh, 20, 47
Athay, R. G. 1976, The Solar Chromosphere and Corona: Quiet Sun (Dordrecht: Reidel)
Athay, R. G., Billings, D. E., Evans, J. W., & Roberts, W. O. 1954, ApJ, 120, 94
Avrett, E. H. 1985, in Chromospheric Diagnostics and Modelling, ed. B. W. Lites (Sunspot, NM: National Solar Observatory), 67
Ayres, T. R. 1981, ApJ, 244, 1064
Ayres, T. R. 2002, ApJ, 575, 1104
Ayres, T. R. 2003, in ASP Conf. Ser. 286, Current Theoretical Models and Future High Resolution Solar Observations: Preparing for ATST, ed. A. A. Pevtsov & H. Uitenbroek (San Francisco, CA: ASP), 431
Ayres, T. R. 2010, HiA, 15, 547
Ayres, T. R., & Linsky, J. L. 1976, ApJ, 205, 874
Beckers, J. M. 1972, ARA&A, 10, 73
Bethge, C., Peter, H., Kentischer, T. J., et al. 2011, A&A, 534, A105
Bjørgen, J. P., Leenaarts, J., Rempel, M., et al. 2019, A&A, 631, A33
Carlsson, M. 2007, in ASP Conf. Ser. 368, The Physics of Chromospheric Plasmas, ed. P. Heinzel, I. Dorotovič, & R. J. Rutten (San Francisco, CA: ASP), 49
Carlsson, M., & Stein, R. F. 1994, in Chromospheric Dynamics, ed. M. Carlsson (Oslo: Institute of Theoretical Astrophysics, Univ. Oslo), 47
Cauzzi, G., Reardon, K. P., Uitenbroek, H., et al. 2008, A&A, 480, 515
Cox, A. N. 2000, in Allen's Astrophysical Quantities, ed. A. N. Cox (4th ed.; New York: AIP Press; Springer)
David, K.-H. 1961, ZAp, 53, 37
Fontenla, J. M., Avrett, E. H., & Loeser, R. 1993, ApJ, 406, 319
Fontenla, J. M., Balasubramaniam, K. S., & Harder, J. 2007, ApJ, 667, 1243
Gingerich, O., Noyes, R. W., Kalkofen, W., & Cuny, Y. 1971, SoPh, 18, 347
Gray, D. F. 2008, The Observation and Analysis of Stellar Photospheres (Cambridge: Cambridge Univ. Press)
Heinzel, P., & Štěpán, J. 2019, in ASP Conf. Ser. 519, Radiative Signatures from the Cosmos, ed. K. Werner et al. (San Francisco, CA: ASP), 59
Judge, P., Tomczyk, S., Hannigan, J., & Sewell, S. 2019, ApJ, 877, 10
Judge, P. G., & Carlsson, M. 2010, ApJ, 719, 469
Judge, P. G., Kleint, L., Leenaarts, J., Sukhorukov, A. V., & Vial, J.-C. 2020, ApJ, 901, 32
Kentischer, T. J., Bethge, C., Elmore, D. F., et al. 2008, Proc. SPIE, 7014, 701413
Kuridze, D., Henriques, V., Mathioudakis, M., et al. 2017, ApJ, 846, 9
Kuridze, D., Mathioudakis, M., Heinzel, P., et al. 2020, ApJ, 896, 120
Kuridze, D., Mathioudakis, M., Morgan, H., et al. 2019, ApJ, 874, 126
Kuridze, D., Socas-Navarro, H., Koza, J., & Oliver, R. 2021, ApJ, 908, 168
Leenaarts, J. 2020, LRSP, 17, 3
Leenaarts, J., Carlsson, M., & Rouppe van der Voort, L. 2012, ApJ, 749, 136
Libbrecht, T. 2016, PhD thesis, Stockholm Univ.
Lites, B. W. 1983, SoPh, 85, 193
Löfdahl, M. G., Hillberg, T., de la Cruz Rodríguez, J., et al. 2021, A&A, 653, A68
Loughhead, R. E. 1969, SoPh, 10, 71
Machado, M. E., & Linsky, J. L. 1975, SoPh, 42, 395
Maltby, P., Avrett, E. H., Carlsson, M., et al. 1986, ApJ, 306, 284
Mauas, P. J. D. 2000, ApJ, 539, 858
Neckel, H. 1999, SoPh, 184, 421
Nikolsky, G. M. 1970, SoPh, 12, 379
Pazira, H., Kiselman, D., & Leenaarts, J. 2017, A&A, 604, A49
Pope, T., & Schoolman, S. A. 1975, SoPh, 42, 47
Rutten, R. J. 2002, JAD, 8, 8
Rutten, R. J., & Uitenbroek, H. 2012, A&A, 540, A86
Scharmer, G. B. 2006, A&A, 447, 1111
Scharmer, G. B., Bjelksjo, K., Korhonen, T. K., Lindberg, B., & Petterson, B. 2003a, Proc. SPIE, 4853, 341
Scharmer, G. B., Dettori, P. M., Lofdahl, M. G., & Shand, M. 2003b, Proc. SPIE, 4853, 370
Scharmer, G. B., Narayan, G., Hillberg, T., et al. 2008, ApJL, 689, L69
Shine, R. A., Milkey, R. W., & Mihalas, D. 1975, ApJ, 199, 724
Shoji, M., Nishikawa, T., Kitai, R., & Ueno, S. 2010, PASJ, 62, 927
Solanki, S. K., Livingston, W., & Ayres, T. 1994, Sci, 263, 64
Tei, A., Gunár, S., Heinzel, P., et al. 2020, ApJ, 888, 42
Uitenbroek, H. 2001, ApJ, 557, 389
Vernazza, J. E., Avrett, E. H., & Loeser, R. 1981, ApJS, 45, 635
Wedemeyer, S., Freytag, B., Steffen, M., Ludwig, H. G., & Holweger, H. 2004, A&A, 414, 1121
White, O. R. 1963, ApJ, 138, 1316
Wiedemann, G., Ayres, T. R., Jennings, D. E., & Saar, S. H. 1994, ApJ, 423, 806